Available online at www.sciencedirect.com
SCIENCE DIRECT®
Computers and Structures 82 (2004) 1719–1736
Computers & Structures
www.elsevier.com/locate/compstruc

Dynamic FE analysis of South Memnon Colossus including 3D soil–foundation–structure interaction

Sara Casciati *, Ronaldo I. Borja

Department of Civil and Environmental Engineering, Stanford University, Stanford, CA 94305-4020, USA

Received 9 July 2003; accepted 10 February 2004
Available online 15 June 2004

Abstract

A full three-dimensional dynamic soil–foundation–structure interaction (SFSI) analysis of a famous landmark in Luxor, Egypt, the South Memnon Colossus, is performed to investigate the response of this historical monument to seismic excitation. The analysis is carried out using the finite element (FE) method in time domain. The statue comprising the upper structure is modeled using 3D brick finite elements constructed from a photogrammetric representation that captures important details of the surface and allows the identification of probable zones of stress concentration. The modeling also takes into account the presence of a surface of discontinuity between the upper part of the statue and its fractured base. FE models of the foundation and the surrounding soil deposit are constructed and coupled with the statue model to analyze the seismic response of the entire system incorporating dynamic SFSI effects. These studies are useful for future conservation efforts of this historical landmark, and more specifically for designing possible retrofit measures for the fractured base to prevent potential collapse of the monument from overturning during an earthquake.

Keywords: Soil–foundation–structure interaction; Multi-body deformable contact; Non-linear dynamic finite element analysis

1. Introduction

The Memnon Colossi are two huge statues (18 m) built in Thebes by the pharaoh Amenothep III (18th Dynasty) to guard the entrance of an ancient mortuary temple on the eastern side of the river Nile, now known as the city of Luxor (Fig. 1). The statues resemble the pharaoh sitting on his throne in regal position with his hands on his knees; his wife, Tiyi, and his mother, Moutemouisa, stand at the sides of the throne in smaller scales. They were called the Colossi of Memnon in Greek times, when they decided that the statues represented their hero, Memnon. He was a king of Ethiopia and son of the the dawn god Eos, who died in the hands of Achilles. After an earthquake in 27 B.C., one of the statues on the northern side produced a musical sound under certain weather conditions. Egyptians thought this sound came from the gods, and Greeks thought it was Memnon's voice. Unfortunately, two centuries later (199 A.D.) the Roman emperor Settimio Severo repaired the damaged statue, and since then the sound has never been heard again. The earthquake and several floods have since wiped out most of the other ruins of the temple, and now only these monuments and the soil remain.

The interest in the south statue arises from its original and unaltered but severely damaged state. In particular, the blocks comprising the base of the statue are severely fractured and must be fastened together or the entire structure could topple during an earthquake.

* Corresponding author. Address: Department of Structural Mechanics, University of Pavia, Via Ferrata 1, Pavia 27100, Italy. Tel.: +39-0382-505458; fax: +39-0382-528422.
E-mail address: fabio@dipmec.unipv.it (S. Casciati).

0045-7949/$ - see front matter
doi:10.1016/j.compstruc.2004.02.026

Fig. 1. South (left) and North (right) Memnon Colossi in Luxor, Egypt.

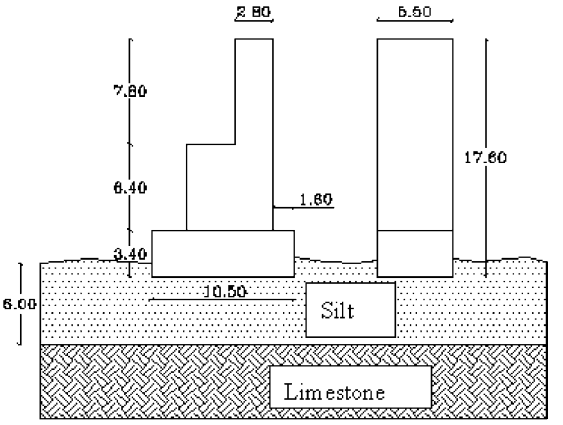

Fig. 2. Model by Verdel and co-workers showing the monument represented by three parallelepipeds.

Remedial measures have been proposed to fix the problem, including stitching the blocks together by shape memory alloy devices in the form of wires. However, planning a good retrofit operation requires careful and accurate modeling of the seismic response of the structure. We believe that with the advances in computational methods it is now possible to predict with reasonable accuracy the seismic demands on this geometrically complex monument. Specifically, computer modeling and simulations are very useful tools for identifying regions of stress concentration where only non-invasive techniques are allowed. Accurate quantification of stresses are also useful for understanding the direction of crack propagation and for quantifying the seismic demands on whatever new materials may be introduced in the retrofit program.

The only computational modeling known to the authors of the seismic response of the South Memnon Colossus was the FE analysis by Verdel and co-workers [1–3]. The statue was represented by three parallelepipeds, one representing the base and two representing the upper structure, resulting in an overestimation of the volume of the statue by about 30% (Fig. 2). The underlying foundation was represented by elastic layers of silt and limestone 6 and 24.5 m in thickness, respectively. The analysis utilized a vertical plane of symmetry between the two statues so that only one statue had to be analyzed. Strictly speaking, the assumed symmetry limits the validity of the model to seismic motions parallel to the plane of symmetry, which serves as a reflecting boundary and therefore is incapable of transmitting seismic waves. To incorporate the effect of contact separation and frictional sliding on the base, El Shabrawi and Verdel [3] carried out a 2D discontinuous modeling by dividing the structue into four blocks and using the distinct element method to handle the interaction between adjacent blocks. Apart from the coarse FE discretization of the statue, a main shortcoming of the Verdel model is the lack of a seismic hazard analysis that resulted in gross oversimplification of the input seismic excitation.

The objective of this paper is to present a modeling technique for analyzing the seismic response of the South Memnon Colossus including the accompanying dynamic soil–foundation–structure interaction, or SFSI. The scope of the present studies is limited to the seismic response of the unaltered structure alone and does not include the assessment of any proposed stabilization measure. The analysis is based on a detailed finite element (FE) modeling of the statue based on photogrammetric survey data made available by the German Cultural Center, which is working at the site for rescue and restoration of the remains of the destroyed temple. The mass of the upper part of the Colossus cannot be estimated with good accuracy unless the volume definition is refined, and hence a significant portion of the paper addresses the relevant issues pertaining to 3D solid mesh generation for an accurate rendering and surface definition of the statue.

The monument was built by pulling the statue on its base so that the entire structure is actually made up of two bodies in contact on a surface. The presence of the contact surface helps in the energy dissipation during an earthquake, but it also alters the structural response and thus it must be included in the FE model. In these studies, a numerical procedure for the simulation of contact behavior is used to capture the opening condition and frictional sliding that may take place during the course of the solution. The opening condition depends on the relative movement of the objects, while the friction condition depends on the contact force and the friction coefficient of the contact surface. This creates non-linearity in the FE solution, and thus we resort to a time-domain FE analysis with Newton iteration to advance the solution incrementally in time.

An Egyptian agency, Sabry and Sabry (see Ref. [4]), carried out a geotechnical investigation at the site, and wrote a soils report in Arabic. Diagrams with English legends suggest that boreholes were drilled in close proximity to the two statues. Penetration tests published in the soils report reveal a soils profile consisting of an alluvium layer of clayey silt and silty clay approximately 6 m thick, underlain by a deposit of compacted limestone. The site is subject to regular flooding, and thus the soil could potentially undergo liquefaction during very strong earthquakes. However, the seismicity in the Luxor area suggests that very strong earthquakes enough to liquefy the underlying soil deposit are highly unlikely at the site, and thus in this study we simply assume that the soil deposit will not liquefy. Nevertheless, we still bracket the soils response by the two extreme cases of drained and undrained loading conditions to better understand the possible effect of the presence of fluids in the soil on the overall structural response.

A significant part of the studies addresses the aspect of dynamic SFSI. Conventional analysis applies the seismic excitation at the base of the structure, but current understanding suggests that this may not be accurate in cases where the structure rests on a compressible soil or where the properties of the foundation may alter the response of the structure (such as the presence of cracks). An accurate, though more computationally demanding, approach would be to analyze the entire system as a whole, which includes modeling the structure, foundation, and the surrounding soil, and then predicting the response of the entire system [5]. In this paper, we pursue this latter more refined approach using a 3D FE modeling technique proposed specifically by Borja and co-workers [6–9] to capture SFSI effects. The next section discusses an earthquake source model that generates a seismic excitation that is then used as input into the SFSI model.

2. Earthquake source model for Luxor

Egypt is part of the North-African plate which, historically, has been moving north-east. Said [10] suggested that Egypt can be divided into four major tectonic regions: the Craton Nubian-Arabian Shield, the Stable Shelf, the Unstable Shelf, and the Suez-Red Sea regions. The city of Luxor is geologically part of the Stable Shelf characterized by alluvium deposits at the sides of the river Nile, and surrounded by Oligocene, Eocene, and Miocene areas covered by sand deposits. Underneath the Memnon Colossi are silt layers of low shear strength about 6 m thick resting on a compacted limestone of the Shelf.

Egypt is one of very few regions in which evidence of seismic activities had been documented over the past five thousand years. However, due to the concentration of the population around the sides of the river Nile, there is a lack of documentation in the western and eastern parts of the desert, and all of the information are concentrated on seismic events in the Nile valley. Instrumentation and data acquisition in Egypt began in 1899 with the establishment of the Observatory of Helwan. In 1982, after the Assuan earthquake, a radio telemetric network was inaugurated to monitor the micro-seismic activities in the artificial lake of Nasser. Until very recently, the earthquake-recording network in Egypt relied on the data collected from only four standard seismograph stations. No acceleration recording devices were present until 1997, with the exception of 15 seismic high-gain instruments that were installed around the High Dam after the 1981 Kalabsha earthquake to monitor the seismic activity within the area. The recent project of installing a national network for earthquake monitoring is still ongoing. Furthermore, the faulting structure is not quite identified. The major faults have yet to be mapped and their detailed characteristics have not yet been determined.

Based on the available seismic and tectonic information, and according to the seismic hazard studies found in the literature [4], Egypt is classified as a region of moderate seismicity with high return periods. In particular, the recent Egyptian records report only perceptible earthquakes, which did not cause substantial damage. With the assistance of seismologist Marcellini, we have therefore selected a reference earthquake for the site of Luxor of magnitude 5.5 at a distance of 100 km and developed an input ground motion for the present study.

The computation of the representative ground motion to be used as input for the dynamic analyses of a structure at a particular site can be approached by several methods, whose nature can range from fully probabilistic to fully deterministic [11]. The choice of the approach depends in general on two factors: the available data and the type of problem to be solved. In the case of Egypt, the amount of available data is not sufficient to feed a deterministic model, and the uncertainty and variability related to a sparse and poor strong motion database do not guarantee the reliability of a probabilistic approach. Furthermore, the lack of acceleration–time history records does not allow the match of an existing earthquake with a target parameter. Hence, the simulation of realistic artificial ground motions at the given site is the main issue to be solved. For this purpose, an intermediate approach, which uses some deterministic information about the seismic source and seismic wave propagation together with stochastic procedures, is adopted.

The hybrid stochastic approach, such as the one proposed by Boore [12], is an intermediate method that takes into account both the stochastic nature of

high-frequency ground motions and the physical properties of the source and the travel path. The first task is achieved by considering a time sequence of band-limited random Gaussian white noise, while the second is obtained by assuming a physically based model such as the one proposed by Brune [13] for the source spectrum and the travel path. This method can capture important characteristics of actual ground motions. In particular, the frequency content of the ground motion depends on the earthquake magnitude, accounting for the fact that large earthquakes produce larger and longer-period ground motions than do smaller earthquakes. The frequency content of an earthquake also changes with distance; as seismic waves travel away from a fault, their higher-frequency components are scattered and absorbed more rapidly than their lower-frequency components. As a result, the shifting of the peak of the Fourier amplitude spectrum to lower frequencies (or higher periods) occurs, i.e., the predominant period increases with increasing distance. This is taken into account by applying a travel path operator to the source spectrum. Since the proposed method is based on the mechanics of source rupture and wave propagation, it offers significant advantages over purely empirical methods for magnitudes and distances for which few or no data are available.

In particular, the Boore approach consists of simulating a sequence of values in time to generate a stationary Gaussian White–Noise with limited spectral density function. To achieve a non-stationary process, a time dependent modulating function, $w(t)$, is then applied. Finally, the Fourier spectrum of the resulting signal is multiplied by the source spectrum, $S(f)$, proposed by Brune [14]. Three filters are applied to this spectrum to account for the geometric attenuation, the entire attenuation path, and the decay of the spectral acceleration at high frequencies, respectively.

In the present study, we apply a modified Boore method as follows. The acceleration time history, which has been simulated using a Filtered White–Noise, is made non-stationary in amplitude by means of the modulation function

$$w(t) = at^b \mathrm{e}^{-ct} H(t), \tag{1}$$

where $w(t)$ is the modulation function proposed by Saragoni and Hart [15], and $H(t)$ is the Heaviside function. The coefficients a, b, and c are chosen so that the temporal sequence is normalized, and they refer to the duration of the motion $T_\mathrm{d} = 1/f_\mathrm{c}$, where f_c is the corner frequency in the displacement Fourier amplitude spectrum. The Fourier amplitude spectrum of the resulting signal is then multiplied by the spectrum, $A(f,R)$, defined by

$$A(f,r) = S(f)\frac{1}{R}\mathrm{e}^{-k\pi f}\mathrm{e}^{-\pi R/\beta Q}, \tag{2}$$

where $S(f)$ is the far field spectrum; k accounts for the inelastic attenuation; Q is the quality factor and accounts for the mechanism of diffusion of the secondary waves (it is inversely proportional to the damping ratio of the rock); R is the hypocentral distance and $1/R$ models the geometric spreading; and β is the shear wave velocity.

The spectrum at the seismic source is derived from the Brune model as

$$S(f) = \frac{F_\mathrm{s}\langle R_{\vartheta,\varphi}\rangle P}{4\pi\rho\beta^3} M_0 \frac{(2\pi f)^2}{1+(f/f_\mathrm{c})^2}, \tag{3}$$

where F_s is an amplification factor for the free-surface effect, which implies a zero shear discontinuity (for the case where only shear waves are considered, $F_\mathrm{s} = 2$); $\langle R_{\vartheta,\varphi}\rangle \approx 0.55$ depends on the radiation pattern; $P = 1/\sqrt{2}$ accounts for partitioning the energy into two horizontal components; M_0 is the seismic moment, which, under the assumption of planar rupture, is given by $M_0 = \mu\overline{U}A$, where μ is the strength of the material along the fault, or the modulus of rigidity; A is the rupture area; $\overline{U}$ is the average amount of slip; and ρ is the average mass density of the medium. The spectra for different earthquakes are functions of the seismic moment M_0 and the corner frequency f_c, which can be expressed as

$$f_\mathrm{c} = 4.9 \times 10^6 \beta \left(\frac{\Delta\sigma}{M_0}\right)^{1/3}, \tag{4}$$

where β is in km/s, M_0 is in dyne cm, and $\Delta\sigma$ is the stress drop in bars.

Note that the predicted Fourier spectra vary with magnitude. As a result, the strong influence of the magnitude on both the amplitude and the frequency content of the motion is well reflected. As the magnitude increases, the amplitude and the bandwidth of the resulting signal increase and the corner frequency decreases, implying that more low frequency (long period) motion will occur. This is in agreement with the fact that larger earthquakes produce larger and longer-period ground motions compared to smaller earthquakes.

The above procedure has been implemented into a FORTRAN code by Marcellini et al. [16] for seismic simulation of high-frequency ground motion. The input values are summarized in Table 1. A shear wave velocity $\beta = 3.2$ km/s and a mass density $\rho = 2.7$ q/cm^3 are reasonable for a Cratonic zone (Stable Shield). For the quality factor a frequency dependent attenuation is adopted in the form $Q = qf^n$, with $q = 100$ and $n = 0.8$. The parameter k is highly dependent on the local geologic conditions and can vary from 0.1 to 0.01 depending on the soil type. Since the computed input motion refers to the shaking expected at the bedrock, the parameter k is fixed at 0.01, which is a common value for hard rock.

Table 1
Seismologic input data for the generation of the accelerogram at the site

Parameter	Units	Value
Seismic moment	dyne cm	1995E+25
Moment magnitude		5.50
Corner frequency	Hz	0.5781
Stress drop	bar	100.0000
Duration t_d	s	6.73
Shear wave velocity	km/s	3.20
Mass density	g/cm^3	2.70
Attenuation quality factor $Q = Q_0 f^n$	Hz	$n = 0.800$ $Q_0 = 100$
Attenuation inelasticity factor	s	$k = -0.0100$
Distance	km	100
Amplification function		$0 \rightarrow$ NO
Number of points		2048
Sampling rate		0.0100

With the above input data the seismic hazard model generates a suite of acceleration–time histories among which the one shown in Fig. 3, together with its amplitude Fourier spectrum, is henceforth used as the reference, or base, ground motion for the present study. The acceleration–time history of Fig. 3 must be interpreted as the expected ground motion at the top of the limestone layer (bedrock) in the absence of local soil effects. This particular record has 2048 acceleration values, 4096 Fourier transform values, a time interval of 0.01 s, a maximum acceleration (PGA) of 0.034 g, and a maximum cut-off frequency of 25 Hz. The low value of PGA does not include the effect of local soil condition, which is shown in the next section to amplify the input ground motion (Fig. 4).

To account for more severe ground motions, the hybrid stochastic procedure has been repeated for earthquakes of higher return periods. Let T be the return period of the computed base ground motion of magnitude 5.5. We simulated with Boore method the earthquakes of return periods $2T$, $4T$, and $10T$, corresponding to magnitudes of 5.85, 6.2, and 6.65, respectively. Fig. 5 shows the acceleration time histories simulated at the bedrock of the Colossi site and Table 2 summarizes their main characteristics. Note that both the amplitude and the frequency content of the signal vary with the magnitude. In contrast, the common practice of simply scaling up the amplitude of the base ground motion by a positive scalar coefficient $\lambda \in [1, \infty)$ (see Ref. [17]) represents only the influence of the magnitude on the amplitude, while it fails to account for differences in important characteristics such as frequency content and duration [5].

The value of the return period T of the base ground motion cannot be computed unless the coefficients of the (bounded) Gutenberg–Richter recurrence law are given. For example, if we assume $a = 2.3$, $b = 0.91$, and $M_{max} = 7.5$ [18] for the zone of Red Sea at 100 km from Luxor, we find that the return period of an earthquake of magnitude $M = 5.5$ is $T = 515$ years. However, the suggested maximum magnitude seems to be too high compared with the one obtained from the global hypocenter database for the same area, $M_{max} = 4.9$ [19]. The variability of the available seismic data demonstrates that, in this case, a probabilistic approach would not be reliable and the hazard estimate would strictly depend on the set of data considered. Furthermore, it is worth noting that the 474-years return period is a conventional value commonly adopted for hazard analyses conducted with the purpose of seismic classification for common

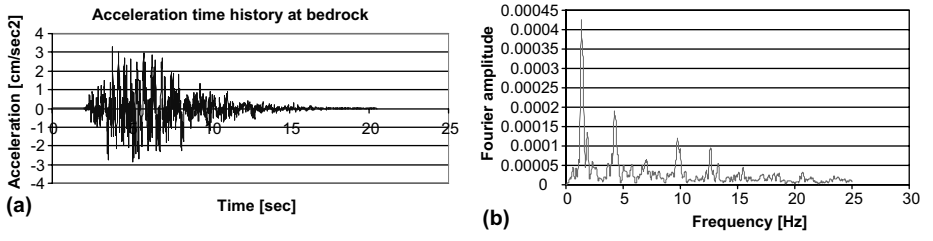

Fig. 3. Input seismic excitation at the Luxor bedrock for the reference ground motion of $M = 5.5$ at 100 km distance: (a) acceleration–time history; (b) Fourier amplitude spectrum.

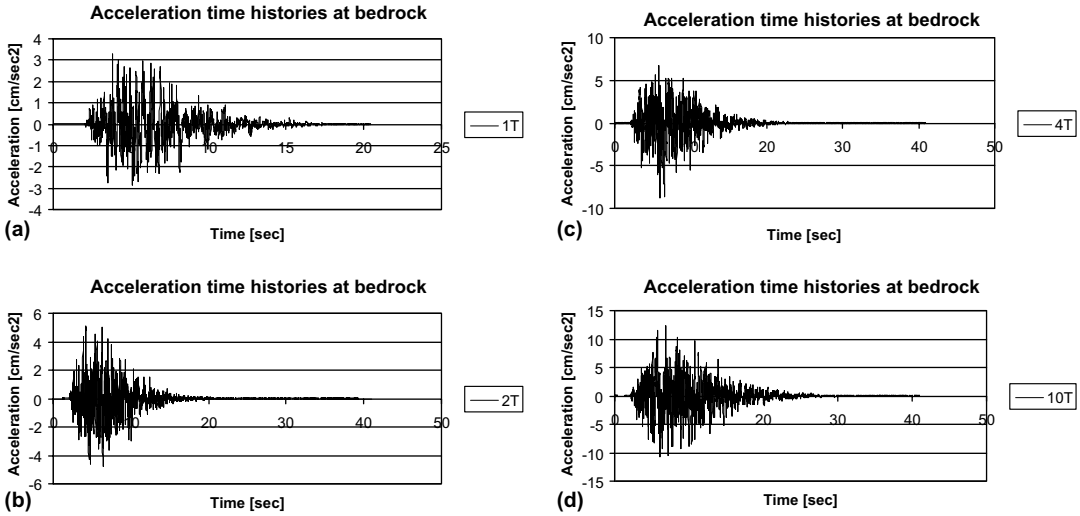

Fig. 4. Input seismic excitation at the Luxor bedrock for different return periods: (a) T; (b) $2T$; (c) $4T$ and (d) $10T$.

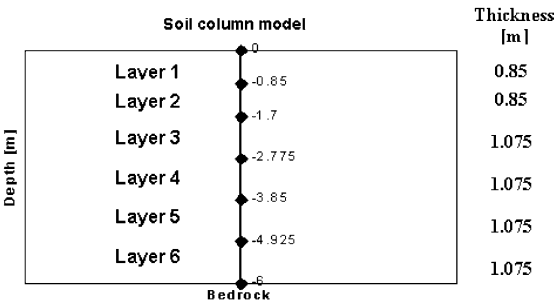

Fig. 5. Soil column model.

buildings. In the case of an important structure, such as a very ancient historical monument, a higher return period is considered.

3. Local site response

The method described in the preceding section models the reference ground motion for Luxor at the bedrock of compacted limestone without taking into account the local soil conditions. However, as seismic waves travel away from the source they reflect and refract on the boundaries between geologic materials, and by the time they reach the ground surface they propagate nearly in the vertical direction. Hence, it is customary to analyze the local site response using one-dimensional ground response models. The term '1D response' is not quite precise as the word 'dimension' simply pertains to the direction of wave propagation (vertical), but the body waves still could have all three components of motion. Several 1D site response models are available in the literature, including those based on an equivalent linear analysis (e.g., SHAKE [20]) and those based on a fully non-linear analysis (e.g., SPECTRA [6–9]). In the absence of precise information on the soil condition at the site, we shall model the local site response in Luxor using an equivalent linear analysis procedure, and specifically using the computer program SHAKE91 [21].

SHAKE91 uses a vertical column model representing the entire thickness of the soil deposit, in our case the 6 m-thick silt layer at the Collosi site. For a homogeneous linearly elastic soil deposit, so-called transfer functions in analytical form are available relating the input ground motion at the base to the output ground motion at the surface, and in this case it is not necessary to discretize the soil layer. However, soils do experience some form of

Table 2
Acceleration–time histories at the bedrock

Return period	Magnitude	PGA [cm/s^2]	Time [s]	Number of points
T	5.5	3.307992	3.81	2048
$2T$	5.85	5.084917	4.21	4096
$4T$	6.2	−8.702876	6.53	4096
$10T$	6.65	12.340370	6.91	4096

stiffness degradation depending upon the amount of deformation, and thus the soil layer is commonly discretized into smaller segments so that the local degradation effect can be captured accurately. For the silt deposit at the site, we have divided the soil layer into six sublayers as shown in Fig. 5. In view of keeping the same vertical discretization for the 3D FE model of the soil deposit, the upper two sublayers are 0.85 m thick resulting in the statue being embedded 1.7 m into the ground. The remaining four sublayers are 1.075 m thick to achieve the total thickness of 6 m for the silt layer.

The properties of the silt layer at the Collosi site are as follows: total mass density $\rho = 1400$ kg/m^3, undegraded Young's modulus $E = 5$ MPa, and Poisson's ratio $\nu = 0.33$ [4]. The elastic shear modulus is then determined as $G = 1.88$ MPa, and the expected shear wave velocity is estimated as $v_s = 37$ m/s. The value of Poisson's ratio, $\nu = 0.33$, corresponds to a fully drained condition. The Collosi site is located on the eastern side of the river Nile where seasonal fluctuation of the ground water table is common. Under a high water table the silt could undergo undrained deformation and the elastic Poisson's ratio could reach a value close to 0.5. Under this condition, $G = 1.67$ MPa (for the same E) and $v_s = 35$ m/s. These values are not much different from the drained case, and thus, provided the ground motion is not strong enough to cause liquefaction, the drainage condition is expected to have little effect on the shear wave propagation. The very low values of G and v_s for the silt are characteristic of alluvial deposits, but they could have also been influenced by soil disturbance during testing (we have made no attempt to modify these values to account for soil disturbance effects). In contrast, the limestone deposit is much stiffer, with a Young's modulus of $\overline{E} = 12$ GPa, an elastic Poisson's ratio of $\overline{\nu} = 0.21$, and a total mass density of $\overline{\rho} = 2400$ kg/m^3 [4].

As the soil deforms in shear its overall shear stiffness degrades and the hysteresis loop grows wider, resulting in a softer response and increased damping. The dynamic soil properties are thus commonly expressed in the form of shear modulus reduction $G/G_{\max}$ and damping ratio ξ curves, plotted as functions of the shear strain. Unfortunately, such curves are not available for the silt layer at the Collosi site. In this study we assume the modulus reduction and damping ratio curves for clay as described in [22,23] to represent the dynamic properties of the silt layer, and those for rock as described in [20] to represent the dynamic properties of the limestone layer. These curves are shown in Fig. 6. Note that the curves shown in Fig. 6 must be interpreted as 'bands' for purposes of statistical analysis [7], since geotechnical data typically exhibit scattering due to expected variations in the soil properties and local conditions. Thus, results of our site response analyses must not be interpreted as blind predictions but only as representative of those expected at the site.

Fig. 7 shows the amplification function (modulus of the transfer function) for the base ground motion of return period T ($M = 5.5$), and the resulting acceleration–time history of the output ground motion at the surface assuming undrained condition for the silty layer. The local soil condition has amplified the ground motion, specifically the PGA, by more than two times. The peak amplification factor decreases with increasing natural frequencies. The greatest amplification factor occurs approximately at the lowest natural frequency (also known as fundamental frequency), which depends on the thickness of the soil deposit H and the shear wave velocity v_s. For the silt layer, this fundamental frequency is estimated to be about $\omega_0 = \pi v_s/2H \approx 9$ rad/s, or a characteristic site period of about $T_0 = 2\pi/\omega_0 = 0.7$ s. Downhole accelerograms were also generated by SHAKE91 at the nodes of the soil column model to better understand the nature of site amplification and for subsequent use in the SFSI analysis.

The ground response analysis has been repeated for the earthquakes of higher return periods and the

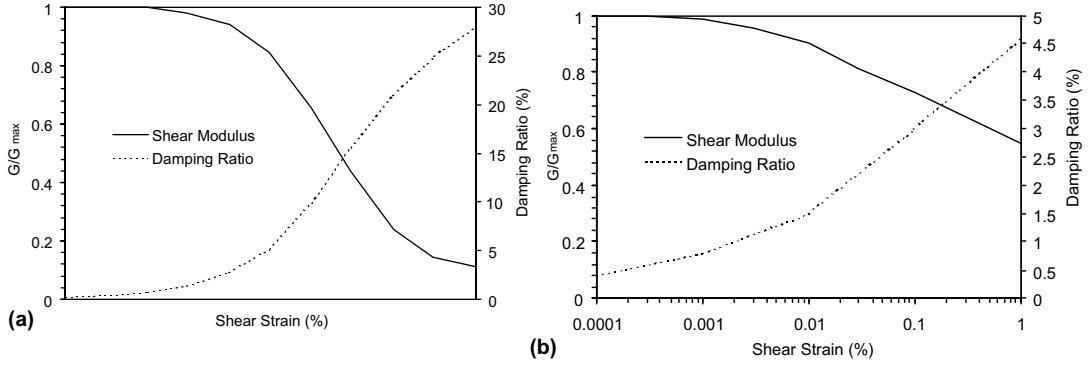

Fig. 6. Assumed modulus reduction and damping ratio curves for: (a) silt layer and for (b) limestone layer [After Sun et al. (1988), Idriss (1990), and Schnabel et al. (1972)].

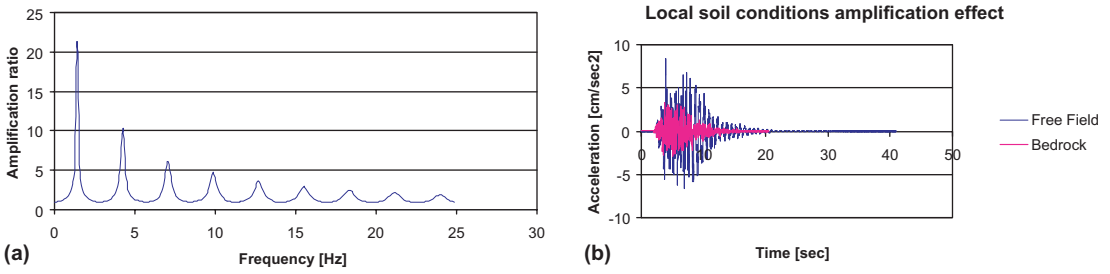

Fig. 7. Output ground motion at free surface for the reference ground motion of $M = 5.5$ at 100 km distance: (a) amplification function and (b) acceleration–time history.

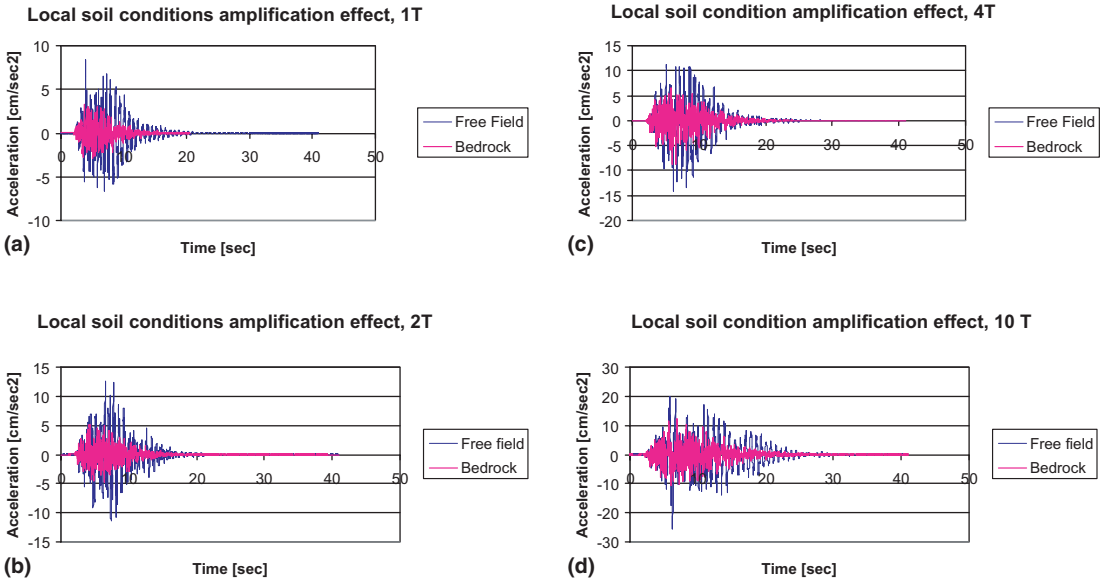

Fig. 8. Output ground motion at free surface for different return periods: (a) T; (b) $2T$; (c) $4T$ and (d) $10T$.

Table 3
Acceleration–time histories at free surface

Return period	Magnitude	PGA [cm/s^2]	Time [s]	Amplification factor
T	5.5	8.428747	3.99	2.547995
$2T$	5.85	12.634280	6.51	2.484658
$4T$	6.2	−14.243150	6.14	1.636603
$10T$	6.65	−25.718880	6.29	−2.084126

resulting acceleration–time histories at free surface are summarized in Fig. 8. Table 3 shows how the frequency content of the input ground motion influences the amplification factor of its PGA value. In particular, the maximum PGA amplification factor (2.55) occurs for the input ground motion of lowest magnitude, while the minimum (1.64) corresponds to the input ground motion of return period $4T$. Also note that the negative values of acceleration become predominant for increasing return periods. As a consequence of the local site condition, the time at which the PGA value occurs has shifted; the predominant period increases for the earthquakes of lower return periods, T and $2T$, while it decreases for the earthquakes of higher return periods, $4T$ and $10T$.

4. SFSI model and method of analysis

The results generated by the analysis of Section 3 are free-field motions that would arise in the absence of the structure. The actual motion at the base of the structure may not necessarily be the same as the free-field motion at the same soil level since it is known that the presence of the structure contaminates the free-field motion. A complete analysis must then include the SFSI effect, where the letter 'F' has been explicitly inserted in the acronym since the foundation, or base, interacts with both the soil and the statue through their contact surfaces.

There are two commonly used methods of SFSI analysis: multistep methods and direct methods [5]. Multistep methods use the principle of superposition to combine the effects of kinematic and inertial interaction, and are limited to the analysis of linear or equivalent linear systems. Direct methods model the entire soil–foundation–structure system in a single step and are more robust than multistep methods, although they are also more computationally demanding. Because of the non-linearities arising from modeling the frictional links at the base, we shall utilize the direct method of SFSI analysis in this study.

Fig. 9 shows four views of the 3D finite element mesh used to model the South Memnon Colossus including its fractured base as well as the surrounding soil medium (the North Colossus is not included in the model). Details of the statue itself are shown in the isometric view of Fig. 10 and are discussed separately in the next section. The structure is mounted on a flat soil region 6 m-thick and supported by the limestone layer, herein considered as the bedrock. Vertical walls on the sides of the soil region form an elliptical boundary around the structure. The soil region is discretized into six horizontal sublayers such that the thicknesses of the sublayers are the same as those of the corresponding vertical segments of the soil column model of Section 3. Essentially, this is done to allow the specification of the previously calculated nodal free-field motions as essential (or Dirichlet) boundary conditions around the soil region, as elaborated further below. Each horizontal slab is then discretized further into elements across its thickness, forming 3D brick finite elements whose centroids are denoted by the symbol '×' in Figs. 9 and 10. The limestone layer is not included in the FE model.

Each of the six horizontal soil slabs was assigned values of the shear modulus G and damping ratio ξ consistent with the effective shear strain level calculated by SHAKE91 at each vertical segment of the soil column model. For example, the effective shear strain in layer n is calculated by SHAKE91 as $\gamma_{n,\mathrm{eff}} = R_\gamma \gamma_{n,\max}$, where $\gamma_{n,\max}$ is the maximum shear strain in the computed shear strain–time history for layer n, and $R_\gamma \approx (M-1)/10$ is a ratio that depends on the magnitude M of the earthquake. The nth soil slab in the 3D mesh is then assigned values of G and ξ corresponding to

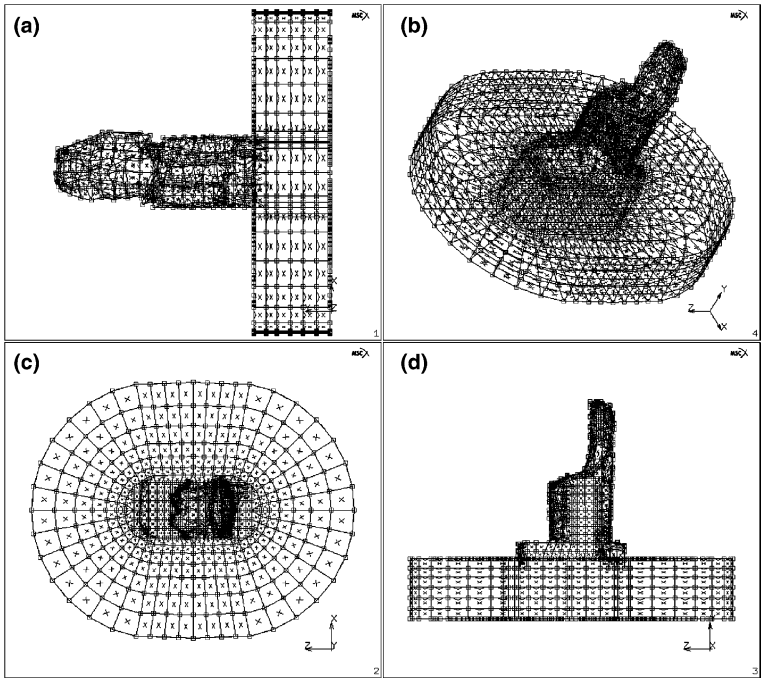

Fig. 9. Four views of the FE model for SFSI analysis: (a) front view; (b) isometric view; (c) plan view and (d) side view.

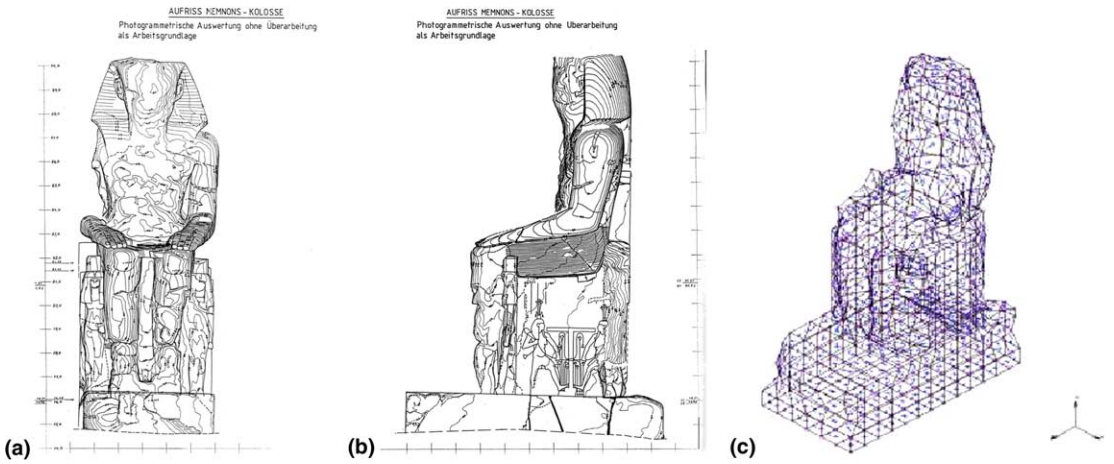

Fig. 10. Photogrammetric survey of the Southern Memnon Colossus: (a) front view; (b) lateral view and (c) isometric view of the FE model.

Table 4
Degradation of the material properties of the soil deposit computed by SHAKE91 for the undrained condition

Accelerogram	Equivalent linear soil properties	Layer					
		1	2	3	4	5	6
T	G [MPa]	1.69	1.66	1.64	1.62	1.61	1.60
	ξ	0.009	0.013	0.018	0.021	0.024	0.025
$2T$	G [MPa]	1.66	1.62	1.60	1.59	1.58	1.53
	ξ	0.012	0.021	0.025	0.027	0.030	0.036
$4T$	G [MPa]	1.66	1.61	1.58	1.55	1.52	1.50
	ξ	0.013	0.024	0.029	0.033	0.038	0.041
$10T$	G [MPa]	1.63	1.54	1.49	1.46	1.40	1.36
	ξ	0.021	0.035	0.043	0.047	0.056	0.062

the effective shear strain level $\gamma_{n,\mathrm{eff}}$. Table 4 shows the values computed by SHAKE91 for the input ground motions of different return periods assuming an undrained condition (Poisson's ratio v close to 0.5). The drained condition leads to a lesser degradation of the shear modulus G, suggesting less damaging effects compared to the undrained case.

We recall that SHAKE91 is an equivalent linear analysis model, and even though it iterates to calculate the effective strain level the converged solution is still based on linear analysis. Our goal is to use the calculated converged elastic soil properties to characterize the 3D soil region. Thus, if the structure is removed and free-field motions are applied on the boundaries of the 3D soil model, then free-field motions will also be created in the interior of the soil region. Therefore, in the presence of the structure any computed deviation from the free-field motion may be attributed directly to SFSI effects.

The FE method accepts the specification of the free-field motion either in the form of a Dirichlet boundary condition (displacement, velocity, acceleration) or in the form of a natural (or Neumann) boundary condition (equivalent nodal forces or surface tractions), but not both. We have a well-defined limestone bedrock, and so we have specified the free-field motion on the base of the soil layer as a Dirichlet boundary condition. On the vertical side walls of the soil region the free-field motion may be applied either as a Neumann boundary condition in combination with the use of non-reflecting boundaries [5] to absorb outgoing waves, or simply as a Dirichlet boundary condition. The latter approach is simpler and reasonably accurate provided the soil region is large enough and the soil boundaries are far enough from the structure. In this study we prescribe the free-field motion as essential boundary conditions and investigate the extent of the FE discretization on the acuracy of the calculated SFSI responses following the procedure described in Ref. [9].

Since the statue was pulled to the top of its base, the foundation–structure system is essentially made up of

two bodies in contact. The presence of a contact can serve as a non-linear damper and thus must be included in the modeling of SFSI. For purposes of specifying the contact, we have assumed the sandstone blocks to be parts of distinct deformable bodies and the contacting surfaces to have a friction coefficient of $\mu = 0.5$, which is typical for sandstone [24–26]. In addition, we have also assumed the base to interact with the surrounding soil, whose elements form another deformable contact body. The contact algorithm ensures that adjacent bodies do not overlap, that there is no interaction between two non-contacting bodies, and that if the bodies are in contact then the zones of contact are governed by the laws of friction.

5. Procedure for 3D solid mesh generation

A photogrammetric representation of the statues has been provided by the German Cultural Center, which is currently working at the site for the rescue and restoration of the remains of the destroyed temple. Fig. 10 shows front and lateral views of the South Memnon Colossus images. The survey, which takes the form of an image of JPG type in raster form, is not recent but is sufficiently accurate. Polylines are superimposed to each level line manually assigning the supporting points, which can be achieved with the software Autocad14 simply by clicking on the mouse. A geo-reference of the images, which pertains to the identification of common points between two planar pictures representing the front and lateral views of the statue, was necessary for an accurate rendering of the 3D images of the solid.

The FE modeling of the structure was carried out using the computer code MARC [27], which runs on SUN workstations SUN Ultra1 and SUN-Blade 1000 under Solaris OS. The selected finite elements are isoparametric eight-noded bricks with tri-linear interpolation functions. Initially, the coarse 3D FE mesh proposed by Verdel [1,2] consisting of three parallelepipeds for the statue was reproduced in MARC. Then, using the photogrammetric surveys, we developed a more refined 3D FE mesh resembling the actual shape of the statue. This was achieved by importing the aforementioned photogrammetric information in the form of polylines into the program MARC and centering the image within the Verdel model. Then the nodes of the external surface of the Verdel model were manually brought to coincide with the points of the polylines through the graphic interface MENTAT. This caused some elements in the Verdel model to be removed and many interior elements to be distorted. The resulting refined mesh for the structure is composed of 1144 nodes and 757 elements (in comparison, the original Verdel description had 1330 nodes and 936 elements).

Severe element distortions could produce ill-conditioning in the mathematical model. For example, some Gauss integration points could fall outside the elements, and some elements could be so distorted as to have aspect ratios well beyond the limits allowed for optimal performance. The program automatically detects this problem and allows the user to manually adjust the nodes to correct the elements with severe geometric distortions. It must be noted that for routine SFSI analysis governed by masses and stiffnesses alone, the need for such a very refined mesh for the structure may not be that important. However, we are presently dealing with a delicate and geometrically complex structure that requires special attention to details. Consider, for example, the fact that the statue's weight was originally estimated at 1070 metric tons by the coarser Verdel model; our more refined rendering estimates the weight of the statue to be 762 metric tons, for a difference of almost 30%. Furthermore, we have identified the absence of material on the posterior part of the base which could produce stress concentrations and instability problems, but not captured by the coarser Verdel model. Obviously, it also would be very difficult to predict the stresses inside the statue itself if the FE mesh was not properly refined. The final 3D FE mesh, including the structure and the underlying soil deposit and shown in Fig. 9, is composed of 3908 nodes, 2977 elements, and 9696 equations.

As for the material properties of the sandstone that make up the Collosus, the material is assumed to be isotropic linear elastic with a Young's modulus of $\widetilde{E} = 20$ GPa, a Poisson's ratio $\widetilde{\nu} = 0.2$, and a mass density of $\widetilde{\rho} = 1800$ kg/m^3 [4]. A modal analysis of the statue alone using these material properties produces the first five frequencies of 12.8, 13.9, 34.7, 38.2, and 47.0 Hz for the structure.

6. Non-linear transient dynamic analyses

Dynamic time-domain FE analyses were carried out by applying the calculated free-field motions all along the Dirichlet boundaries of the soil region. Starting from a stationary initial condition (zero velocity), we prescribed on the Dirichlet boundaries the free-field nodal displacement–time histories obtained by twice integrating the acceleration–time histories computed by SHAKE91. The remaining Neumann boundaries were considered traction-free, including the horizontal ground surface and the exposed surface of the monument. The shaking was applied along the shorter side of the base (lateral or transverse direction with respect to the statue).

The non-linearity in the analyses arises from the contact and friction problems. Contact problems are characterized by two important phenomena: gap opening/closing and friction. The gap describes the contact (gap closed) and separation (gap open) conditions of

two objects (structures). Friction influences the interface relations of the objects after they are in contact. The gap condition is dependent on the movement (displacement) of the objects, and friction is dependent on the contact force as well as on the coefficient of Coulomb friction at contact surfaces. The analysis involving gap and friction was carried out incrementally. Iterations were done in each load–time increment to stabilize the gap-friction behavior. To advance the solution incrementally in time, we employed a full Newton–Rapson iteration algorithm based on a relative displacement tolerance of 0.1.

For time integration the second-order accurate Newmark-beta algorithm with parameters $\gamma = 1/2$ and $\beta = 1/4$ was selected. For linear problems, this method is unconditionally stable and exhibits no numerical damping. However, instability can develop in the presence of non-linearities, which can be circumvented by reducing the time step and/or adding (stiffness) damping. To properly assign the time step, we first decided on the frequencies that are important to the response of the structure. In general, the time step should not exceed 10% of the period of the highest relevant frequency in the structure, otherwise, large phase errors will occur. The phenomenon usually associated with a time step that is too large is strong oscillatory accelerations leading to numerical instability. To circumvent this problem we have repeated the analysis with significantly different time steps (1/5 and 1/10 of the original) and compared the responses. After several trials, we fixed the time step at $\Delta t = 0.01$ s.

Damping represents the dissipation of energy in the structural system. For the direct integration method, the Rayleigh damping model was used in the analysis. The global damping matrix was calculated as a linear

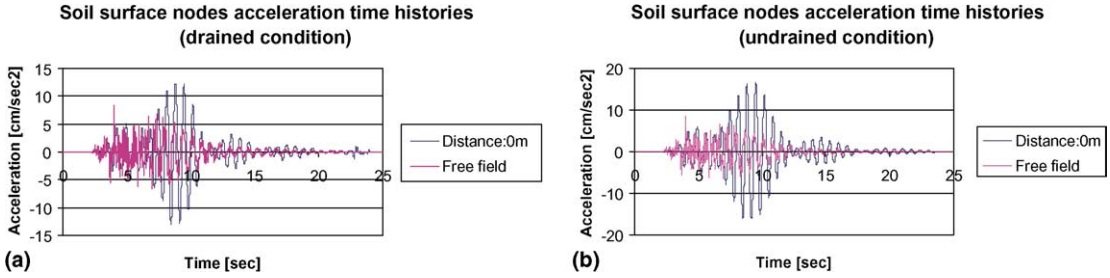

Fig. 11. Comparison of horizontal ground surface accelerations with and without SFSI: (a) Poisson's ratio = 0.33 and (b) Poisson's ratio = 0.499.

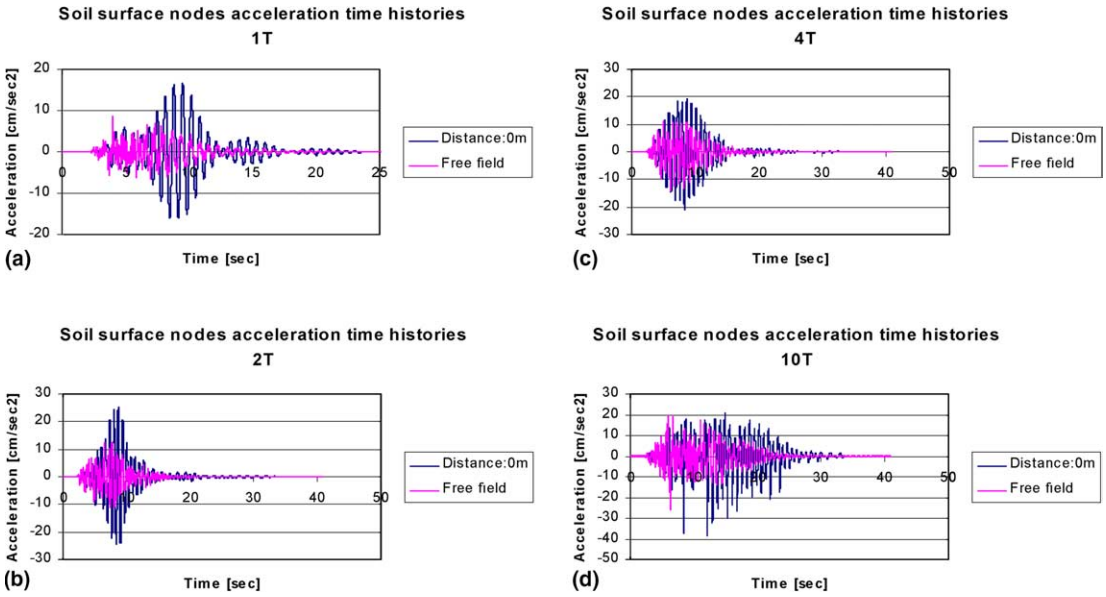

Fig. 12. Comparison of horizontal ground surface accelerations with and without SFSI for different earthquake return periods (Poisson's ratio = 0.499): (a) T; (b) $2T$; (c) $4T$ and (d) $10T$.

Table 5
Acceleration–time histories near the base of the structure

Return period	Magnitude	PGA [cm/s^2]	Time [s]	Amplification factor
T	5.5	16.694	9.5	1.975264
$2T$	5.85	25.425	8.68	2.012382
$4T$	6.2	−20.803	8.33	1.460562
$10T$	6.65	−38.166	12.1	1.483968

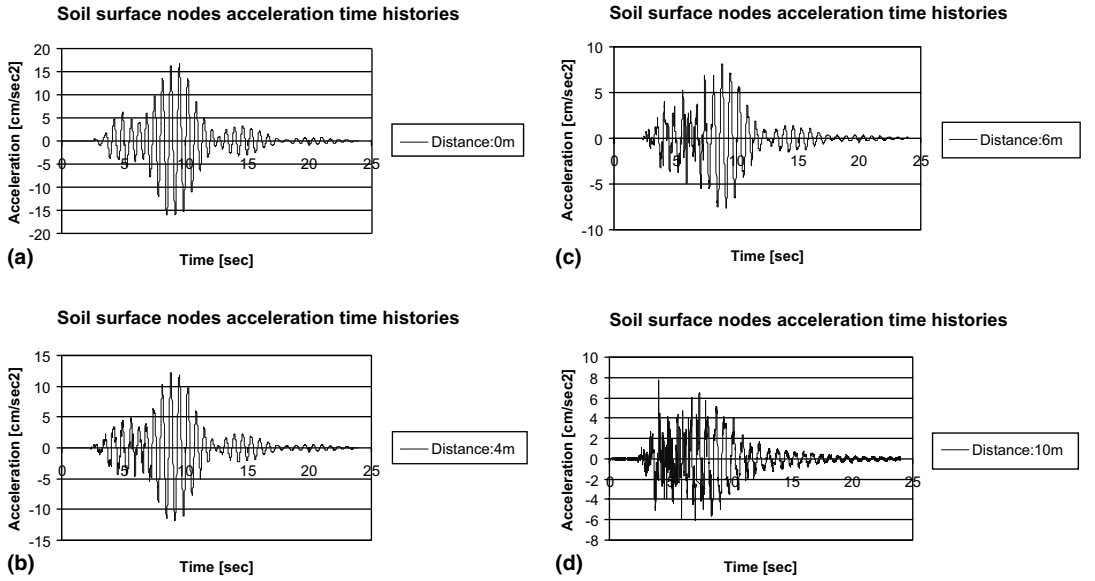

Fig. 13. Comparison of horizontal ground surface accelerations time histories at varying distances from the Colossus, for the accelerogram of return period T: (a) 0 m; (b) 4 m; (c) 6 m and (d) 10 m away from the structure.

combination of the element mass and stiffness matrices through the equation

$$\boldsymbol{C} = \sum_{i=1}^{n} \left[\alpha_i \boldsymbol{M}_i + \left(\beta_i + \gamma_i \frac{\Delta t}{\pi} \right) \boldsymbol{K}_i \right], \tag{5}$$

where $\boldsymbol{C}$ is the global damping matrix; n is the number of elements in the mesh; $\boldsymbol{M}_i$ is the mass matrix of the ith element; $\boldsymbol{K}_i$ is stiffness matrix; α_i is the mass damping coefficient; β_i is the stiffness damping coefficient; γ_i is the numerical damping coefficient; and Δt is the time increment. The stiffness damping coefficients β_i were estimated from an empirical relationship with the damping ratios ξ_i as summarized in Table 4 for the soil deposit. For the sandstone, β_i was assumed to be about 2%. The mass matrix damping coefficient α_i was kept constant at 0.001.

The element stiffness matrix was formed using the standard eight-point Gaussian integration rule, appropriate for eight-noded trilinear brick elements. Element quantities such as stresses and strains were calculated at each integration point. For the nearly incompressible behavior the B-bar approach was used [28].

7. Results and discussions

To reduce the total number of possible combinations of parameters, we first investigated the effect of drainage condition in the silt layer. As mentioned earlier, this entails using two values of Poisson's ratio: $v = 0.33$ for

Table 6
Acceleration–time histories at varying distances from the structure, for return period T

Distance [m]	PGA [cm/s^2]	Time [s]	Amplification factor
0	16.694	9.5	2.162208
4	12.198	8.81	1.584156
6	8.129	8.81	1.055714
10	7.7	4.09	1

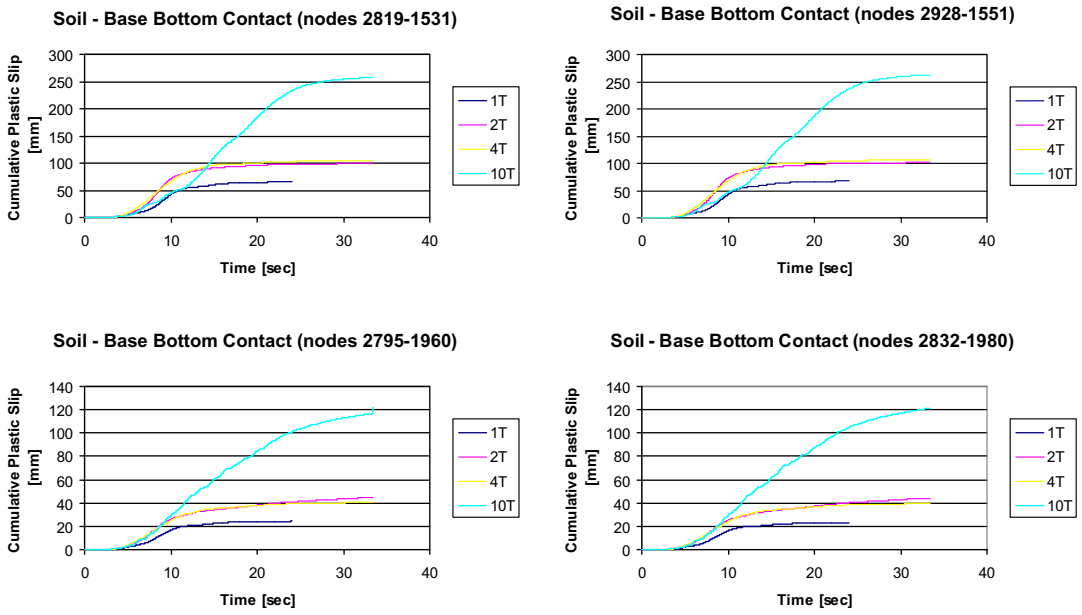

Fig. 14. Cumulative plastic slip at the contact nodes between the statue and the base for different earthquake amplitudes.

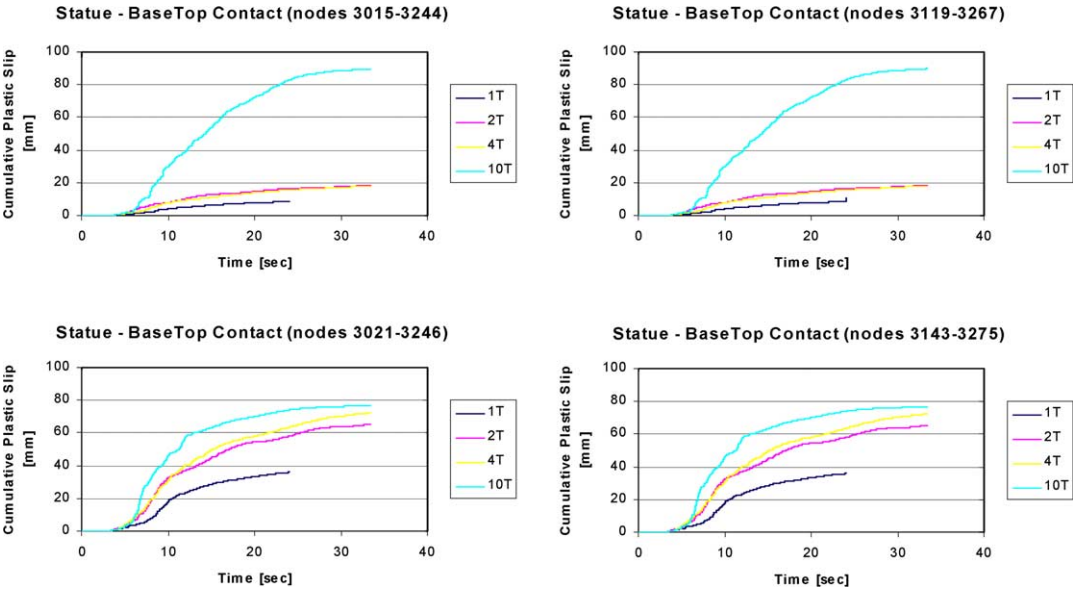

Fig. 15. Cumulative plastic slip at the contact nodes between the base and the soil for different earthquake amplitudes.

the drained case, and $v = 0.499$ for the undrained case. Applying the ground motion in the transverse direction with respect to the statue, we compare in Fig. 11 the effects of Poisson's ratio on the horizontal ground surface accelerations. To elucidate the comparison further, the figure shows both the surface free-field motion and the surface ground motion near the base of the statue. The latter is expected to contain SFSI effects, which is evident from the comparison of the two surface ground motions. Note that the case where $v = 0.499$ results in stronger ground shaking. This is due in part to the fact that for a fixed Young's modulus E the elastic shear modulus G decreases as the Poisson's ratio v increases to 0.5. However, introducing incompressible soil elements

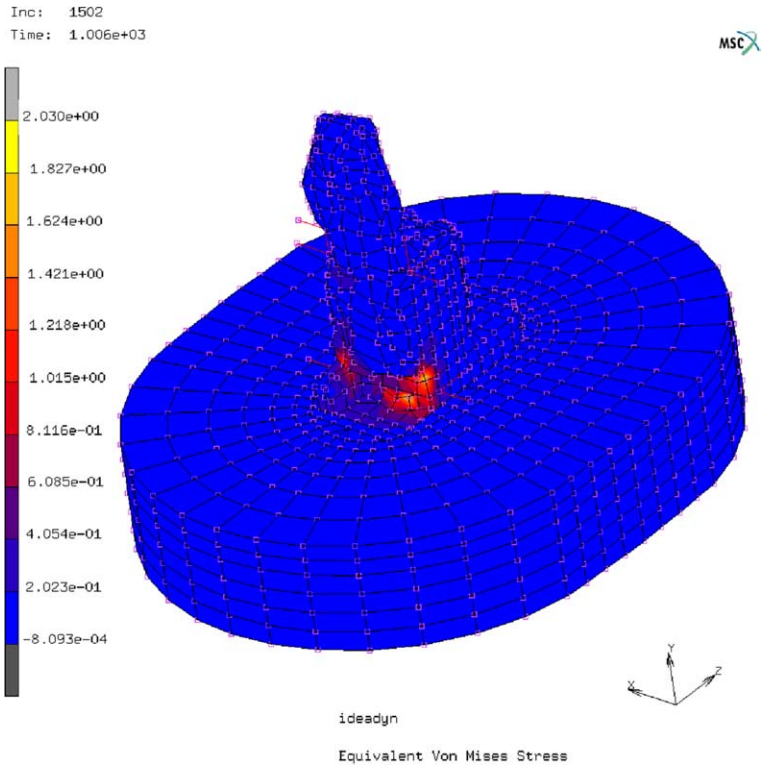

Fig. 16. Von Mises stress distribution in the statue for accelerogram $10T$.

also enhances the sidesway mode but reduces the contribution of the vertical and rocking modes (they become higher frequency modes due to the increased bulk stiffness), thus amplifying the horizontal ground motion. For this reason, we shall focus the analysis on the more critical case of undrained deformation, and hence use $v = 0.499$ for the soil deposit throughout.

Fig. 12 compares the free field motion and the surface ground motion near the base of the statue for earthquakes of different return periods. The maximum absolute values of acceleration increase in the proximity of the statue. The amplification factors of the PGA of the free field motions are summarized in Table 5. The PGA is amplified by a factor of about two for the accelerograms of return periods T and $2T$, and by a factor of about 1.5 for the accelerograms of return periods $4T$ and $10T$. Note that the maximum absolute value of ground motion acceleration corresponding to a return period $2T$ is higher than the one corresponding to a return period of $4T$ near the base of the statue. Also the predominant period of the ground motions increases in the vicinity of the structure.

Next, we investigate the extent of discretized zone on the propagation of scattered waves induced by SFSI effects. Fig. 13 and Table 6 show the surface ground motions at points 0, 4, 6, and 10 m away from the side of the base of the statue, for the accelerograms of return period T. The maximum absolute values of acceleration and the corresponding predominant periods decrease with increasing distance from the statue. The surface ground motion with SFSI approaches the free field ground motion near the vertical side boundaries of the soil, as expected.

To better understand the influence of ground shaking on the interaction between the individual components of the soil–foundation–structure system, we show in Figs. 14 and 15 the cumulative plastic slip at the bottom of the base relative to the underlying foundation soil, and the cumulative plastic slip of the bottom of the statue relative to its base, respectively, as functions of time and earthquake amplitude. These plastic slips represent the cumulative slips at the contact nodes obtained by summing the absolute values of the incremental plastic slips experienced throughout the duration of the analysis. Note that the cumulative plastic slip is not the final distance that one block moves relative to the adjacent block. If at the nth time increment Δt the incremental plastic slip between the two contact nodes is $d_i = \|\Delta \boldsymbol{d}_i\|$, then the cumulative plastic slip is $\sum d_i$. In other words, even if the two blocks returned to their original positions the cumulative plastic slip would still be greater than zero because it represents the total excursion or distance

that the two blocks have traveled relative to each other. Thus, the cumulative plastic slips monotonically increase with time.

The cumulative plastic slip values were sampled at the contact nodes located at the corners of the base bottom and statue bottom, respectively, where the stresses are expected to be high. Note that the cumulative plastic slips reach higher values at the contact nodes in the rear end of the structure, which supports most of the weight of the statue. The cumulative slip curves corresponding to earthquakes with return periods $2T$ and $4T$ are quite similar to each other, while the ones corresponding to return periods of T and $10T$ represent lower and upper bounds to the cumulative slips, respectively. In general, the plastic slips computed at the contact between the bottom of the base and the underlying soil are greater than those computed at the contact between the bottom of the statue and the top of the base.

Finally, Figs. 16 and 17 identify the probable zones of stress concentration in the statue, the supporting base, and the underlying soil foundation during the period of most intense ground shaking for an earthquake of return period $10T$. The figures plot the contours of Von Mises stresses (defined as $\sqrt{3/2}\|\boldsymbol{s}\|$, where $\boldsymbol{s}$ is the deviatoric component of the Cauchy stress tensor $\boldsymbol{\sigma}$ and the symbol $\|\cdot\|$ denotes a tensor norm), a stress measure commonly used to describe the level of shearing in a continuum. As shown in the figures the Von Mises stress values are higher at the contact between the top of the base and the bottom of the statue than at the contact between the bottom of the base and the underlying foundation soil, even though the cumulative plastic slips are lower for the former than for the latter. Representations such as these are useful for designing possible retrofit measures for the monument since they identify regions where the stress demands are likely to be high.

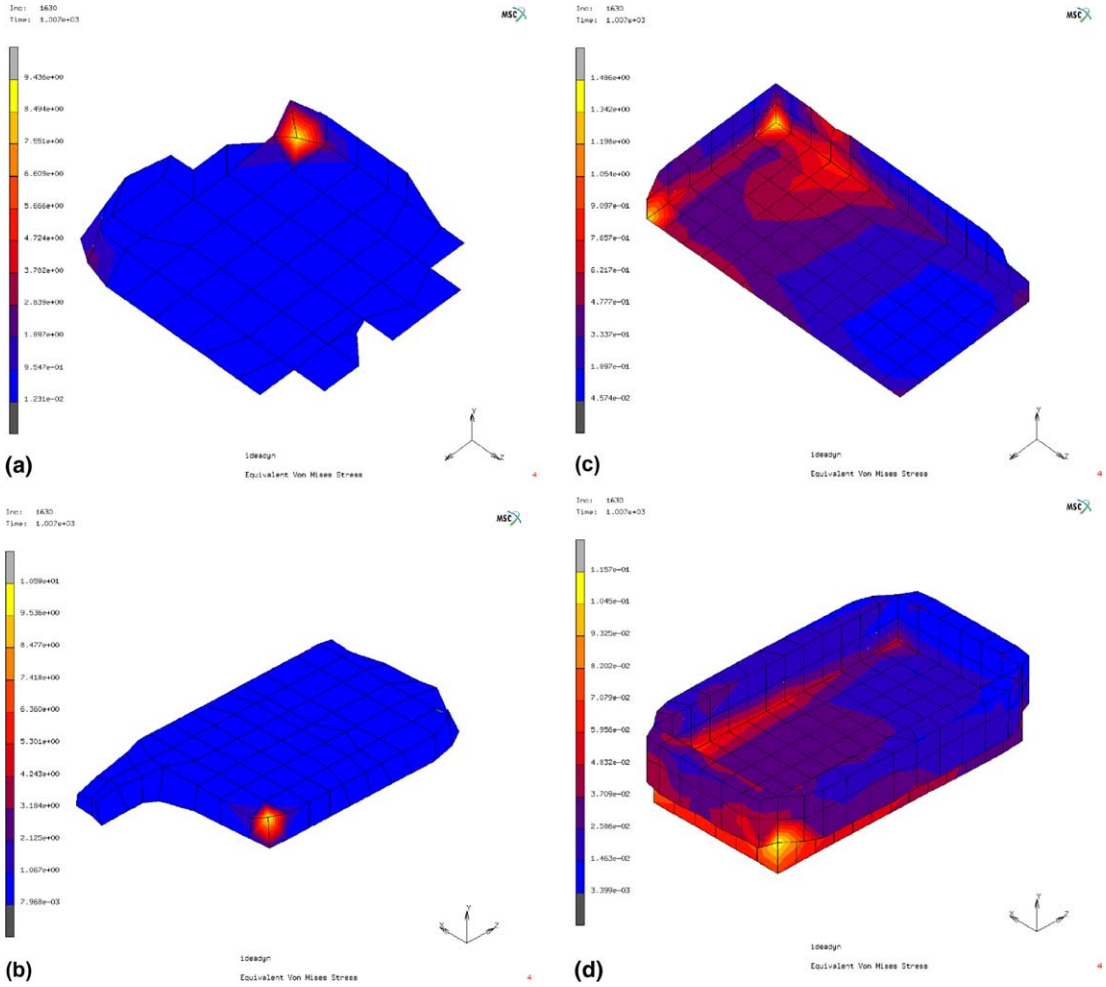

Fig. 17. Details of the Von Mises stress distribution for accelerogram $10T$, at various locations: (a) statue bottom; (b) base top; (c) base bottom and (d) soil foundation top.

8. Summary and conclusions

We have presented a methodology for non-linear dynamic SFSI analysis of an important landmark, the South Memnon Colossus in Luxor, Egypt, as it responds to artificially generated earthquakes of different return periods. The methodology involves a consistent framework for seismic hazard analysis applicable to important structures located in developing countries where data are scarce if not completely lacking. Apart from our interests in quantifying the seismic response of this particular structure for educational purposes as well as for investigating possible retrofit measures for the fractured foundation base, we have carried out these detailed studies in an attempt to combine, in a systematic fashion, different aspects of earthquake engineering analysis with available analytical and computational modeling tools. The modeling included the use of a hybrid stochastic approach for generating synthetic earthquakes of different return periods based on the seismicity of the region, the analysis of the local site response based on available soils data, and the modeling of the SFSI effects using three-dimensional time-domain non-linear FE analysis. The studies demonstrate how different solution methodologies may be used in tandem to analyze complex earthquake engineering problems.

Acknowledgements

Financial support for this research was provided in part by National Science Foundation under contract no. CMS-02-01317 through the direction of Dr. Clifford S. Astill. Funding for the first author was provided by a research assistantship from the John A. Blume Earthquake Engineering Center. The authors are grateful to Dr. Alberto Marcellini of University of Pavia for assistance with the generation of the earthquake source model for Luxor; to Drs. David Pollard and Atilla Aydin of Stanford University for providing some insight into the mechanical properties of fault zones; and to an anonymous reviewer for his/her constructive review.

References

[1] Verdel T. Géotechnique et monuments historiques, méthodes de modélisation appliquées à des cas égyptiens [in French]. Phd thesis, INPL-Ecole des Mines, Nancy, France; 1993.
[2] Verdel T. Stability of the Colossus of Memnon: preliminary geotechnical study. Nancy, France: Ecoles des Mines; 1991.
[3] El Shabrawi A, Verdel T. The seismic risk on ancient masonry structures by the use of the distinct element method. Unrefereed paper; 1993.
[4] Casciati S. Analisi di pericolosità, fragilità sismica ed ipotesi di adeguamento per uno dei colossi di Memmone [in Italian]. Msd thesis, Department of Structural Mechanics, University of Pavia, Italy 2001.
[5] Kramer SL. Geotechnical earthquake engineering. Englewood-Cliffs, NJ: Prentice-Hall; 1996.
[6] Borja RI, Duvernay BG, Lin CH. Ground response in lotung: total stress analysis and parametric studies. J Geotechn Geoenviron Eng ASCE 2002;128:54–63.
[7] Borja RI, Lin CH, Sama KM, Masada GM. Modelling non-linear ground response of non-liquefiable soils. Earthquake Eng Struct Dyn 2000;29:63–83.
[8] Borja RI, Chao HY, Montáns FJ, Lin CH. Nonlinear ground response at Lotung LSST site. J Geotechn Geoenviron Eng ASCE 1999;125:187–97.
[9] Borja RI, Chao HY, Montáns FJ, Lin CH. SSI effects on ground motion at Lotung LSST site. J Geotechn Geoenviron Eng ASCE 1999;125:760–70.
[10] Said R. The geology of Egypt. Brookfield, Rotterdam: A.A. Balkema; 1990.
[11] Casciati F, Casciati S, Marcellini A. PGA and structural dynamics input motion at a given site. J Earthquake Eng Eng Vibrat 2003;2:25–33.
[12] Boore D. Stochastic simulation of high-frequency ground motions based on seismological model of the radiated spectra. Bull Seismol Soc Am 1983;73:1865–94.
[13] Brune J. Tectonic stress and the spectra of seismic shear waves from earthquakes. J Geophys Res 1970;75:4997–5009.
[14] Brune J. Correction. J Geophys Res 1971;76:5002.
[15] Saragoni R, Hart G. Simulation of artificial earthquakes. Earthquake Eng Struct Dyn 1974;2:249–67.
[16] Marcellini A, Daminelli R, Franceschina G, Pagani M. Regional and local seismic hazard assessment. Soil Dyn Earthquake Eng 2001;21:415–29.
[17] Vamvatsikos D, Cornell CA. Incremental dynamic analysis. Earthquake Eng Struct Dyn 2002;31:491–514.
[18] Riad S, Yousef M. Earthquake hazard assessment in the southern part of the western desert of Egypt. Report submitted to the National Authority for Remote Sensing and Space Sciences. Center of Studies and Research for the South Valley Development Assuit University; 1999.
[19] US Geological Survey. Global hypocenter data base—version 3. United States Geological Survey, National Earthquake Information Center; 1994.
[20] Schnabel PB, Lysmer J, Seed, HB. SHAKE—a computer program for earthquake response analysis of horizontally layered sites. EERC Report No. 72-12, Earthquake Engineering Research Center, University of California at Berkeley, CA; December 1972.
[21] Idriss I, Sun JI. SHAKE91—a computer program for conducting equivalent linear seismic response analyses of horizontally layered soil deposits. Center for Geotechnical Modeling, University of California at Davis, CA; November 1992.
[22] Sun JI, Golesorkhi R, Seed HB. Dynamic moduli and damping ratios for cohesive soils. Report No. UCB/EERC-88/15, Earthquake Engineering Research Center, University of California at Berkeley, CA; 1988.

[23] Idriss I. Response of soft soil sites during earthquakes. In: Proceedings of the Memorial Symposium to Honor Professor Harry Bolton Seed, Berkeley, CA, vol. II; May 1990.
[24] Barton N. Review of a new shear-strength criterion for rock joints. Eng Geol 1973;7:287–332.
[25] Byerlee J. Friction of rocks. Pure Appl Geophys 1978;116: 615–26.
[26] Dieterich JH, Kilgore BD. Direct observation of frictional contacts: new insights for state-dependent properties. Pure Appl Geophys 1994;143:283–302.
[27] MARC vol. A: Theory and user information, version 7.3; August 1998.
[28] Hughes TJR. The finite element method. Englewood-Cliffs, NJ: Prentice-Hall; 1987.